SUPPLEMENTAL MATERIAL

Quantitative Intravascular Biological Fluorescence-Ultrasound Imaging of Coronary and Peripheral Arteries *In Vivo*

Dmitry Bozhko, MS[X]*, Eric A. Osborn, MD PhD[YZ]*, Amir Rosenthal, PhD[X], Johan W. H. Verjans, MD PhD[Y], Tetsuya Hara, MD PhD[Y], Jason R. McCarthy, PhD[Y], Stephan Kellnberger, PhD[XY], Georg Wissmeyer, MS[X], Saak V. Ovsepian, PhD[X], Adam Mauskapf, BS[Y], Ashley F. Stein, MD[Y], Farouc A. Jaffer, MD PhD[Y§], Vasilis Ntziachristos, PhD[X§]

[X] Helmholtz Zentrum München, Institute for Biological and Medical Imaging, 85764 Neuherberg, Germany; Munich School of Bioengineering, Technische Universität München (TUM), 81675 Munich, Germany;

[Y] Cardiovascular Research Center and Cardiology Division, Massachusetts General Hospital, Harvard Medical School, Boston, MA

[Z] Cardiology Division, Beth Israel Deaconess Medical Center, Harvard Medical School, Boston, MA

* Drs. Bozhko, and Osborn share first authorship

[§] Drs. Jaffer and Ntziachristos share senior authorship

SUPPLEMENTAL METHODS AND RESULTS

Supplemental Information S1. Characterization of cNIRF-IVUS system in vitro

NIRF resolution and sensitivity. To investigate the NIRF resolution and the sensitivity of the cNIRF-IVUS system, a tube filled with a NIR fluorophore (AlexaFluor 750) was fixed at an arbitrary angle to the cNIRF-IVUS catheter. Such a phantom allowed measurements of the NIRF signal from precisely controlled distances. First, the NIRF sensitivity was assessed as function of the distance in saline or blood (**Supp. Fig. 1a**). As expected, due to higher absorption and scattering, the sensitivity drop was sharper in blood (red line). Nevertheless, 200 nM of NIR fluorophore was detectable at distances < 2 mm. while the sensitivity limit of the system was designated to SNR=2.5. Next, NIRF resolution was measured through calculation of the full width at half maximum (FWHM) of the NIRF signal from the fluorescent tube (**Supp. Fig. 1b**, red and blue dots). The angular resolution at 1 mm distance in blood is 24°. These data are in line with results reported previously (1).

Ultrasound resolution. The ultrasound resolution of the cNIRF-IVUS system is determined by the geometry and frequency of the ultrasound transducer. A copper wire (100 μm diameter) was imaged at different distances using the 9F/15MHz and 4.5F/40MHz cNIRF-IVUS catheters to measure the lateral and axial ultrasound resolutions (**Supp. Fig. 1b**). At a typical imaging distance of 2 mm, the 4.5F/40MHz catheter demonstrated ~2 × better lateral resolution compared to the 9F/15MHz catheter: 270 μm and 500 μm, respectively (green and magenta triangles). The axial resolution was not affected by distance and was measured to be 150 μm and 240 μm for the 4.5F/40MHz and 9F/15MHz catheters, respectively. These results are similar to those reported for commercial 40 MHz IVUS systems (2): 100 μm axial, 250 μm lateral.

Supplemental Information S2. Method of NIRF signal correction for blood attenuation

We assumed that that the fluorescence is generated at the luminal border of the arterial wall based on prior data demonstrating that plaques provide markedly less attenuation of NIRF signals compared to blood (3). Thus, it could be considered, that the excitation light and emitted fluorescence propagate only through attenuating blood between the vessel wall and optical fiber. Therefore, detected optical power *P* can be modelled by the equation

$$P = P_0 C R / \alpha(r), \quad \text{(Eq. 1)}$$

where P_0 is the illumination power at the tip of the fiber, *C* is the unknown concentration of the fluorophore within illuminated volume, *R* is a constant related to optical properties of the imaged fluorescent probe such as absorption coefficient and quantum yield, and, finally, $\alpha(r)$ is the blood related distance-dependent light attenuation function. From Eq. 1, the fluorophore concentration can be found as

$$C = \frac{P\alpha(r)}{P_0 R}. \quad \text{(Eq. 2)}$$

As evident from Eq. 2, parameter P_0R scales the concentration linearly if no quenching occurs. In practice, system calibration for P_0R is required for the specific probe imaged. Otherwise, the measured concentration *C* may only be represented in arbitrary units. Therefore, calibration was done by relating the NIRF signal to the known imaging distance and concentrations of the fluorophore for *in vivo* phantom measurements (i.e. **Supp. Fig. 2b**).

In case of measurements in saline, the function $\alpha(r)$ can be modelled by the Beer-Lambert law. However, light propagation through blood is diffusive due to photon scattering, and therefore the Beer-Lambert law is not applicable. We instead used the theory introduced by Twersky for transmission measurements (4), which is often applied to model light transmission through blood in biological applications (5–7). The Twersky theory describes the light intensity transmitted through blood in terms of its optical and physiological parameters, allowing the distance-dependent attenuation in blood to be expressed as:

$$\alpha(r) = e^{-r(\mu_{a1}+\mu_{a2})}\left(e^{-B\omega(1-\omega)2r} + q\left(1 - e^{-B\omega(1-\omega)2r}\right)\right), \quad \text{(Eq. 3)}$$

where μ_{a1} and μ_{a2} are the absorption coefficients of blood at the excitation and emission wavelengths, respectively, that can be derived from the extinction coefficients provided in Bosschaart et al. (8) ω is the fractional hematocrit of blood. B represents scattering, and q is a constant parameter related to the detection system. Here, B and q were defined empirically by curve fitting the experimental data to the expression given in Eq. 3.

It should be considered that noise in the detected signal P might be amplified by the correction formula (Eq. 2) and lead to spurious signals. Therefore, we employed a regularization function β that suppresses correction for signals below the noise level to minimize their subsequent amplification:

$$C = P\beta\alpha(r)/P_0R \quad \text{(Eq. 4)}$$

β is a function of the detected signal P and could be described by Eq. 5.

$$\begin{cases} \beta = 32\left(\frac{P}{P+P_{noise}} - \frac{1}{2}\right)^2, & if\ P \le 3P_{noise} \\ \beta = 1 - 32\left(\frac{P}{P+P_{noise}} - \frac{1}{2}\right)^2, & if\ P > 3P_{noise} \end{cases} \quad \text{(Eq. 5)}$$

where P_{noise} is the noise level of the detected signal. Once the distance-dependent attenuation function $\alpha(r)$ is found (i.e. **Supp. Information S3**), Eq. 4 can be used for attenuation correction of the NIRF signals.

Supplemental Information S3. cNIRF-IVUS measurements of distance-related blood attenuation ex vivo and in vivo.

Given the success of intravascular NIRF imaging of coronary-sized arteries through blood, we hypothesized that blood attenuation in vivo might be less severe then attenuation measurements derived from ex vivo blood attenuation properties. Therefore, rather than relying on the *ex vivo* attenuation values measured or found in the literature, we derived a new correction algorithm exclusively based on *in vivo* blood attenuation measurements obtained from living swine (see below).

<u>*Ex vivo* cNIRF-IVUS measurements of blood attenuation</u>. To determine the distance-attenuation function $\alpha(r)$ *ex vivo*, we employed the setup shown in **Supp. Fig. 2a**, in which measurements were performed while submerged in saline or *ex vivo* blood. cNIRF-IVUS image acquisition was performed at an angle to a fluorescent tube. By correlating ultrasound-measured distances with

NIRF intensities, the attenuation function $\alpha(r)$ was computed (**Supp. Fig. 2e**) for saline (blue dots) and swine blood *ex vivo* (green dots).

In vivo cNIRF-IVUS measurements of blood attenuation. To define the distance-attenuation function $\alpha(r)$ *in vivo*, we analysed cNIRF-IVUS signals obtained from the vessel wall of a living swine (MGH IACUC Protocol #2012N000066) injected locally with a NIR fluorophore (AlexaFluor 750). Experimental procedures are described in the manuscript Methods section entitled "Validation of cNIRF-IVUS *in vivo*" and illustrated in **Fig. 2**. The NIRF *in vivo* readouts are presented in **Supp. Fig. 2e** (red dots). As evident from the **Supp. Fig. 2e**, NIR light attenuation by *in vivo* blood was significantly less than that observed by *ex vivo* blood. This finding could be related to differential oxygenation levels of blood (9,10), the presence of blood flow *in vivo* (10–12), and/or the effect of absorption flattening (13,14). The Twersky model fits the curve corresponding to *in vivo* blood measurements with R^2=0.98 when parameters q=0.32 and B=24.9. In this work we assumed blood absorption to be consistent throughout the arterial circulation. One potential limitation to this approach is that the optical properties of blood can very influenced by the blood velocity variations present in different arterial beds, with slower blood velocity resulting in higher light absorption. According to published data (10), blood flow-based variations in optical attenuation are relatively small and do not exceed 12%. Therefore, the computed distance-attenuation function $\alpha(r)$ is anticipated to reasonably correct *in vivo* NIRF signals acquired from both the carotid and coronary arteries.

To validate the developed distance-correction algorithm we performed a test cNIRF-IVUS scan using the setup shown in **Supp. Fig. 2a**. The raw NIRF image of a fluorescent tube containing a

constant NIR fluorophore concentration before correction is shown in **Supp. Fig. 2c**, demonstrating a decrease in NIRF signal as the catheter distance increases in relation to the tube. Sequentially, distance-correction was applied to the raw NIRF image using the distance-attenuation model $\alpha(r)$ measured in saline. As expected, distance correction allowed recovery of uniform NIRF signal intensities over the entire pullback, consistent with the known constant concentration of NIR fluorophore in the capillary tube (**Supp. Fig. 2d**).

The results of **Supp. Fig. 2c** and **d** confirm the ability to perform distance-related attenuation correction of fluorescence intensities given that the attenuation function $\alpha(r)$ is known. However, it was unknown if the cNIRF-IVUS system could be employed to dynamically characterize blood attenuation of optical signals during an *in vivo* experimental measurement. For this reason, we investigated the sensitivity of cNIRF-IVUS to variations in hematocrit (HCT) levels *in vivo*, using a phantom consisting of a flexible fluorescent tube containing AlexaFluor 750 placed next to the catheter as shown in **Supp. Fig. 2b**. The overall diameter of the tube – catheter phantom was 2.6 mm, i.e. small enough to insert it to the aorta of living pig through a 9F introducer.

Furthermore, we showed that cNIRF-IVUS can detect changes in the attenuation of blood (**Supp. Fig. 2f**) due to, for example, haematocrit variations. *In vivo* measurements of the phantom arrangement were performed under normal, physiological HCT levels (blue dots **Supp. Fig. 2f**), and then repeated following sequential dilution of blood with intravenous normal saline boluses that resulted in a lower HCT=25% (green dots in **Supp. Fig. 2f**). HCT levels were confirmed by independent HCT blood analysis (MGH Core Laboratory). Lines in **Supp. Fig. 2f** represent fits

to the Twersky model. The ability to obtain real-time individualized blood correction curves can be used to more accurately quantify NIRF under varying physiological conditions. The algorithm is only applicable to a hybrid system, whereby exactly co-registered measurements of fluorescence intensity (by NIRF) and of distance (by IVUS) are introduced in a global minimization problem, which solves for blood attenuation and aids in building a per-vessel distance calibration curve corresponding to the *in vivo* settings.

Phantom measurements confirmed the ability of the cNIRF-IVUS system to track signal attenuation related to blood absorption. To investigate if blood-attenuation changes can be monitored *in vivo* during intravascular measurements and adjusted without use of a phantom, we analysed cNIRF-IVUS imaging data from healthy blood vessels. **Supp. Fig. 3** presents cNIRF-IVUS data obtained *in vivo* from an intact artery after systematic administration of a NIR fluorescent agent. We discovered a low-frequency varying fluorescence intensity component (**Supp. Fig. 3a-c**) that inversely correlates with the catheter – vessel wall distance (**Supp. Fig. 3**). This signal is attributed to the background wall fluorescence and could be employed to dynamically estimate blood attenuation measurements *in vivo*. **Supp. Fig. 3a** and **b** show representative examples of the fluorescence distribution in an uninjured vessel. Note, here that the dynamic range of the colormap was scaled to make NIRF signal variations visible. **Supp. Fig. 3c** displays a NIRF-IVUS cross-sectional image in polar coordinates, where the vessel wall and catheter are outlined by red and magenta lines, respectively. By plotting the fluorescence intensity values normalized for beam size at a corresponding distance, we obtained the attenuation function $\alpha(r)$ *in vivo* (**Supp. Fig. 2**). These measurements confirm the ability of cNIRF-IVUS to retrieve the attenuation function $\alpha(r)$ *in vivo* without *a priori* knowledge of the

blood parameters present in the imaging catheter environment. This strategy can be employed to dynamically monitor against changes of blood attenuation, such as due to blood hematocrit or oxygen state variations.

Supplemental Information S4. cNIRF-IVUS imaging of a healthy vessel.

To confirm the specificity of the in vivo NIRF fluorescence signal, normal healthy arteries were imaged with the 4.5F/40 MHz cNIRF-IVUS catheter. The imaging protocol utilized was identical to that described in "Intravascular cNIRF-IVUS in vivo imaging of arterial disease" in the manuscript.

Supp. Fig. 4a and **b** show cNIRF-IVUS images of a normal LAD coronary artery in a healthy pig without administration of NIR fluorophore. NIRF background signal concentration was calibrated relative to AlexaFluor750 look-up table. Quantitative analysis of the detected *in vivo* NIRF signal in a normal coronary artery demonstrated a low NIRF background signal that was ~35-fold less than that measured in an animal injected with NIRF fluorophore into the artery wall shown in **Fig. 2**, and ~100-fold less NIRF signal than measured for targeted NIRF fibrin imaging of an implanted coronary stent in **Fig. 4**. **Supp. Fig. 4c** and **d** display cNIRF and IVUS image from the non-injured distal femoral artery of a pig following systemic administration of ICG (0.25 mg/kg), with *in vivo* cNIRF concentration signals quantitatively calibrated for ICG. **Supp. Fig. 4e** and **f** present typical cNIRF-IVUS cross sectional images. Note, in contrast to the focal high *in vivo* NIRF signals observed in **Fig.2**, **Fig 3,** and **Fig. 4**, low diffuse NIRF signal with no distinctive NIR fluorescence pattern was detected from all uninjured and uninjected arteries, confirming the specificity of the *in vivo* NIRF fluorescence signal.

Supplemental Information S5. Validation of angioplasty induced injury model.

In addition to the experiments described in "*In vivo cNIRF-IVUS imaging of peripheral arterial injury induced by angioplasty*" in the main paper, the angioplasty vascular injury model was further validated with additional *in vivo* imaging studies performed in the femoral artery using the 4.5F/40MHz cNIRF-IVUS catheter and detailed histological correlation (N=2; **Supp. Fig. 5**). After obtaining antegrade intra-arterial access with a 6 French introducer sheath in the common iliac artery, vascular injury was performed in the distal femoral artery using a 4.0 × 20mm angioplasty balloon inflated to 10 atm for 1 min three times. Subsequently, ICG (0.25 mg/kg) was administered intravenously, followed by Evans blue (EB; 50 ml of 5% solution) 30 min later, to assess impaired endothelial permeability. Ninety minutes after ICG injection, 40 mm cNIRF-IVUS pullbacks were performed in triplicate across the injured zone. After sacrifice, the injured vessel was harvested on ice and multichannel *ex vivo* fluorescence microscopy (FM) (Kodak ImageStation 4000, Carestream Health) performed for white light (WL), autofluorescence (FITC, excitation/emission 470/535 nm), Evans Blue (Cy5, excitation/emission 630/700 nm), and ICG (Cy7, excitation/emission 740/790 nm). The tissue was then freshly frozen in optimal cutting temperature compound and serial 7μm cryostat sections obtained. Tissue cross-sections were evaluated by fluorescence microscopy (Nikon Eclipse 90i) for autofluorescence, Evans Blue, and ICG. Matched adjacent histological cross-sections were stained for elastin with Verhoeff-Van Gieson (VVG; Elastic Stain Kit HT254; Sigma-Aldrich) to identify disruptions of the elastic lamina, followed by immunohistochemistry to detect endothelial damage (CD31 clone LCI-4, 1:100 dilution; Santa Cruz Biotechnology) using a MACH2 labeled AP polymer secondary visualized with Vulcan fast red chromagen (Biocare

Medical). Co-registration between cNIRF-IVUS, standalone IVUS, and histological cross-sections was performed using fiducial markers.

Supplemental Information S6. Imaging of fibrin deposition on coronary artery stents.

To further understand the *in vivo* cNIRF-IVUS imaging experiments on NIRF fibrin-coated coronary artery stents described in "*In vivo* intracoronary cNIRF-IVUS of fibrin deposits on coronary stents", we performed additional fluorescence imaging and histology analyses. Clinical grade bare metal stents (Veriflex) were coated with a NIR fluorescent fibrin probe (FTP11) by incubating overnight in experimental blood clots generated with human fresh frozen plasma (Partners Institutional Review Board #2004P001401), $CaCl_2$, thrombin, and FTP11. Two non-overlapping 2.75 × 12 mm clinical bare metal stents coated with the FTP11-containing clots were implanted in the right coronary artery of a normal, healthy pig, guided by x-ray angiography and IVUS. At sacrifice, the coronary artery was isolated on ice, and the stents were immediately harvested for digital photography and FRI (Kodak ImageStation 4000, Carestream Health) with white light (WL), autofluorescence (FITC, excitation/emission 470/535 nm), and FTP11 (Cy7, excitation/emission 740/790 nm)). The stents were then longitudinally opened by cutting through the stent and tissue with sharp scissors, and the stent material manually extracted. The tissue was freshly frozen in optimal cutting temperature compound, and sectioned into 7μm sections with a cryostat. Tissue cross-sections were evaluated by fluorescence microscopy (Nikon Eclipse 90i) for autofluorescence (FITC channel) and FTP11 (Cy7 channel), and matched adjacent cross-sections stained with Carstairs' stain for fibrin visualization.

Supplemental Information S7. In vivo cNIRF-IVUS imaging of inflammatory atherosclerosis.

To demonstrate cNIRF-IVUS system to image inflammation, a key driver of plaque complications, we employed a modified New Zealand White rabbit atherosclerosis model (MGH IACUC Protocol #2013N000015) that generates highly-inflamed, aortic plaques (15). Following 2 weeks of high-cholesterol diet (4.7% coconut oil-based, 1% total cholesterol; Research Diets Inc.), the rabbit underwent aortic balloon-injury (3F Fogarty; Edwards Lifesciences) and continued on 1% high-cholesterol diet for 4 weeks followed by 4 weeks of normal cholesterol chow. At 8 weeks post-injury, the rabbit was imaged with cNIRF-IVUS 24 hours after intravenous injection of a protease-activatable imaging reporter (Prosense VM110, 4 mg/kg IV; PerkinElmer). The day of imaging, the rabbit was anesthetized with ketamine (35 mg/kg) and xylazine (3.5 mg/kg), a 5F sheath was placed in the carotid artery and heparin (IV 100 U/kg) was administered. A 70mm cNIRF-IVUS pullback through blood was performed with rotation speed of 120 rpm revealing two areas (12-30mm and 38-50mm at **Supp. Fig. 7a** and **Supp. Fig. 7d**) of elevated NIR fluorescence signal with a 7mm lower NIRF signal region in between. The same fluorescence distribution was observed on the *ex vivo* FRI image of the resected artery (**Supp. Fig. 7e**). Representative cross-sectional cNIRF-IVUS images are shown in **Supp. Fig. 7b** and **Supp. Fig. 7c**.

SUPPLEMENTAL REFERENCES

1. Jaffer FA, Calfon MA, Rosenthal A, Mallas G, Razansky RN, Mauskapf A, et al. Two-dimensional intravascular near-infrared fluorescence molecular imaging of inflammation in atherosclerosis and stent-induced vascular injury. *J Am Coll Cardiol* Elsevier Inc.; 2011;**57**:2516–2526.
2. Elliott MR, Thrush AJ. Measurement of resolution in intravascular ultrasound images. *Physiol Meas* 1996;**17**:259–265.
3. Jaffer FA, Vinegoni C, John MC, Aikawa E, Gold HK, Finn AV, et al. Real-time catheter molecular sensing of inflammation in proteolytically active atherosclerosis. *Circulation* 2008;**118**:1802–1809.
4. Twersky V. Absorption and multiple scattering by biological suspensions. *J Opt Soc Am* 1970;**60**:1084–1093.
5. Steinke JM, Shepherd AP. Role of Light Scattering in Spectrophotometric Measurements of Arteriovenous Oxygen Difference. *IEEE Trans Biomed Eng* 1986;**BME-33**:729–734.
6. Steinke JM, Shepherd AP. Role of Light Scattering in Whole Blood Oximetry. *Ieee Trans Biomed Eng* 1986;294–301.
7. Lipowsky HH, Usami S, Chien S, Pittman RN. Hematocrit determination in small bore tubes by differential spectrophotometry. *Microvasc Res* 1982;**24**:42–55.
8. Bosschaart N, Edelman GJ, Aalders MCG, Leeuwen TG Van, Faber DJ. A literature review and novel theoretical approach on the optical properties of whole blood. *Lasers Med Sci* 2014;**29**:453–479.
9. Friebel M, Helfmann J, Netz U, Meinke M. Influence of oxygen saturation on the optical scattering properties of human red blood cells in the spectral range 250 to 2,000 nm. *J*

Biomed Opt International Society for Optics and Photonics; 2015;**14**:034001.

10. Roggan A, Friebel M, Rschel K Do, Hahn A, Mu Ller G. Optical Properties of Circulating Human Blood in the Wavelength Range 400-2500 nm. *J Biomed Opt* International Society for Optics and Photonics; 1999;**4**:36–46.

11. Friebel M, Müller G, Meinke M, Helfmann J. Influence of shear rate on the optical properties of human blood in the spectral range 250 to 1100nm. *J Biomed Opt* International Society for Optics and Photonics; 2007;**12**:54005.

12. Enejder AMK, Swartling J, Aruna P, Andersson-Engels S. Influence of cell shape and aggregate formation on the optical properties of flowing whole blood. *Appl Opt* Optical Society of America; 2003;**42**:1384–1394.

13. Schneider AS, Harmatz D. An experimental method correcting for absorption flattening and scattering in suspensions of absorbing particles: circular dichroism and absorption spectra of hemoglobin in situ in red blood cells. *Biochemistry* ACS Publications; 1976;**15**:4158–4162.

14. Duysens LNM. The flattening of the absorption spectrum of suspensions, as compared to that of solutions. *Biochim Biophys Acta* 1956;**19**:1–12.

15. Phinikaridou A, Hallock KJ, Qiao Y, Hamilton JA. A robust rabbit model of human atherosclerosis and atherothrombosis. *J Lipid Res* 2009;**50**:787–797.

SUPPLEMENTAL FIGURE LEGENDS

Supplemental Figure 1. Characterization of the NIRF and IVUS signal profiles for cNIRF-IVUS catheters. **(a)** NIRF sensitivity as function of detector-to-target distances measured in blood (red dots) and saline (blue dots). Note, the sensitivity limit of the system was designated to SNR=2.5. **(b)** Lateral resolution of the NIRF and ultrasound detectors measured as function of detector-to-target distance. Red dots represent NIRF resolution in blood, blue dots – NIRF resolution in saline, green triangles – ultrasound resolution of the 4.5F/40MHz catheter, purple triangles – ultrasound resolution of the 9F/15MHz catheter.

Supplemental Figure 2. Measurements of distance attenuation and validation of correction model described in S3. **(a)** Setup arrangement for measurements of $\alpha(r)$ in saline or *ex vivo* blood. **(b)** Setup arrangement for *in vivo* validation of cNIRF-IVUS ability to reveal attenuation changes in blood using a fluorescent tube phantom. NIRF signal from a tube with AlexaFluor 750 detected over increasing catheter-target distance before **(c)** and after **(d)** distance correction (color scale bar: red = high NIRF; blue = low NIRF). **(e)** Distance attenuation model measured in saline (blue), *in vivo* blood (red), and *ex vivo* blood (green). **(f)** Light attenuation due to blood with normal (blue) and low (green) level of haematocrit (HTC) measured *in vivo* with cNIRF-IVUS. Lines represent fits to Twersky model.

Supplemental Figure 3. Attenuation function derived from *in vivo* measurements without *a priori* knowledge of blood parameters. **(a)** NIRF image of a healthy vessel after systemic administration of a NIR fluorescence agent. **(b)** Representative NIRF-IVUS cross-sectional image of a normal, healthy artery segment. **(c)** NIRF-IVUS cross-section converted to polar

coordinates was used to calculate a thickness of blood through which fluorescence was detected. Red and magenta lines outline the catheter and vessel lumen boundaries, respectively. **(d)** Plot of NIRF signal normalized for beam size as a function of the catheter-to-vessel wall distance. All scale bars are 1mm.

Supplemental Figure 4. cNIRF-IVUS images of healthy control arteries *in vivo*. Longitudinal view IVUS image of a non-injected swine LAD coronary artery **(a)** and distal femoral artery **(c)** of a pig after systemic administration of AlexaFluor 750 and ICG, respectively. Corresponding background cNIRF signals **(b)** and **(d)** were acquired simultaneously with IVUS images. Representative cross-sectional cNIRF-IVUS fusion images **(e)** and **(f)** of a LAD coronary artery at pullback position 1 and 2 at (a) and (b). cNIRF signals are calibrated to AlexaFluor 750 (b, e, and f) and ICG (d) concentrations. All scale bars are 1mm.

Supplemental Figure 5. cNIRF-IVUS imaging of angioplasty-induced vascular injury. **(a)** Longitudinal view IVUS image reveals topography of the femoral artery after balloon injury. **(b)** The corresponding cNIRF image map demonstrates elevated *in vivo* NIRF ICG signal focally at the location where balloon injury was performed, with negligible NIRF signal (blue/black pseudocolor) in the flanking non-injured regions. A cross-sectional IVUS image **(c)** at the location of the red dotted line in (a) and (b) shows no apparent vascular injury. **(d)** The fusion cNIRF-IVUS cross-sectional image identifies a focal area of increased NIRF ICG signal (yellow/green pseudocolor at 11 o'clock). **(e)** and **(f)** Multichannel fluorescence microscopy of a tissue cross-section from the location corresponding to the cNIRF-IVUS image shown in (d). The region of the white dotted box in (f) is presented in a magnified view in (e). ICG uptake (red

pseudocolor) associated with Evans Blue (EB, green pseudocolor) signal distinct from autofluorescence (AF, blue pseudocolor) tissue background signal, indicating that the mechanism of ICG entry into the arterial wall was related to an impaired endothelial barrier. White arrowheads in (e) highlight a region of vascular injury from the angioplasty balloon. Scale bars are (e) 250 μm and (f) 500 μm. Histological staining of adjacent matching sections to (e) and (f) confirmed that ICG accumulation occurred where there was **(g)** disruption of the internal elastic lamina (VVG, Verhoeff Van Gieson; black arrowheads indicate injured zone; scale bar, 250 μm) and **(h)** denudation of overlying endothelium (pink = positive CD31 immunostaining; black arrowheads indicate injured zone; scale bar, 100 μm). A control, non-injured femoral artery demonstrated **(i)** no ICG signal uptake by fluorescence microscopy, that was **(j)** associated with an intact endothelial layer by CD31 immunohistochemistry. Scale bars in (i) and (j) are 200 μm.

Supplemental Figure 6. *Ex vivo* imaging of fibrin deposits on coronary stents. **(a)** Angiogram of the right coronary artery (RCA) demonstrate the implanted stents (red lines). Below a photograph **(b)** of the resected coronary artery paired with fluorescence reflectance imaging (FRI) **(c)** for FTP11-fibrin NIRF signal (red pseudocolor) that reveals heterogeneous, stent-associated high NIRF-fibrin signal. **(d)** and **(e)** demonstrate two representative zones of fluorescence microscopy (FM; FTP-11 fibrin = red pseudocolor, autofluorescence (AF) = green pseudocolor) paired with **(f)** and **(g)** showing histological Carstairs staining for fibrin (red = fibrin positive) after manual stent removal. High FTP-11 signal associated with the lumen and areas surrounding stent strut voids (asterisk) due to FTP11- fibrin coated stent deposition. Carstairs reveals overlying areas of platelet-rich thrombus that formed *in vivo* after stent implantation with no detectable NIRF-fibrin signal.

Supplementary Figure 7. *In vivo* cNIRF-IVUS imaging of inflammation in atherosclerosis. **(a)** Fused longitudinal ultrasound (black and white) and cNIRF images of the rabbit atheroma. Representative cNIRF-IVUS cross-sectional images in the pullback position 1 and 2 are shown in **(b)** and **(c)**, with lower left magnified insets demonstrating evidence of atherosclerosis at position 1 in (b). Scale bars, 1 mm for all images. The cNIRF image of inflammatory plaque protease activity **(d)** correlated with the *ex vivo* fluorescence reflectance image (FRI) of the resected artery **(e)**.

SUPPLEMENTAL FIGURES

Supplemental Figure 1

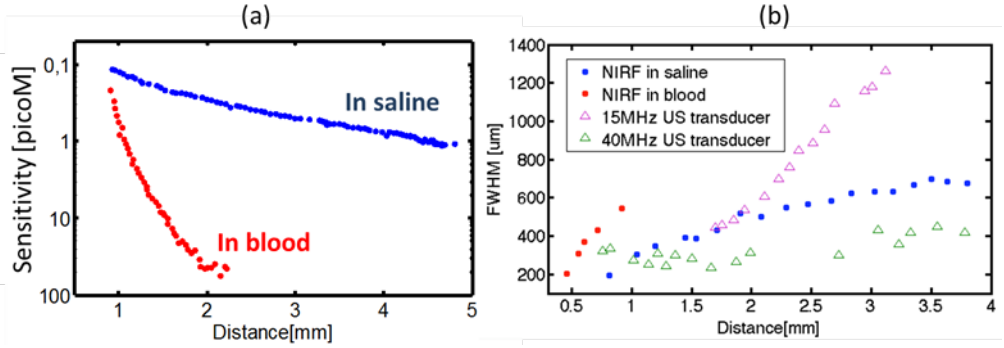

Supplemental Figure 2

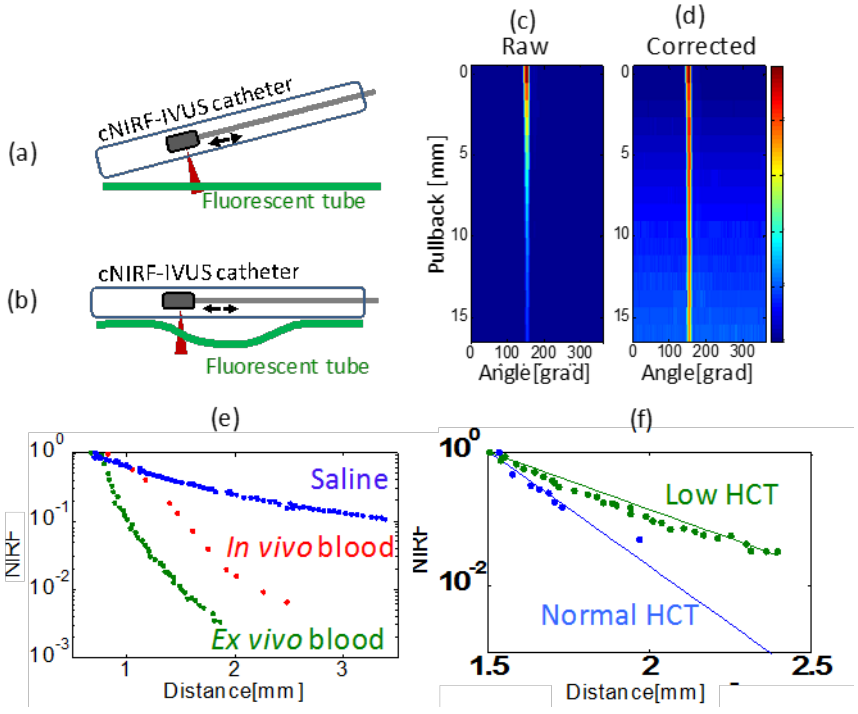

Supplemental Figure 3

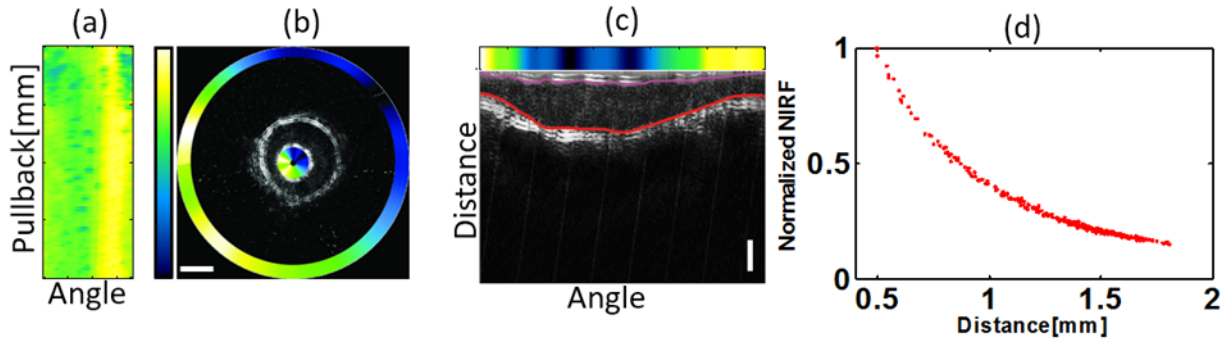

Supplemental Figure 4

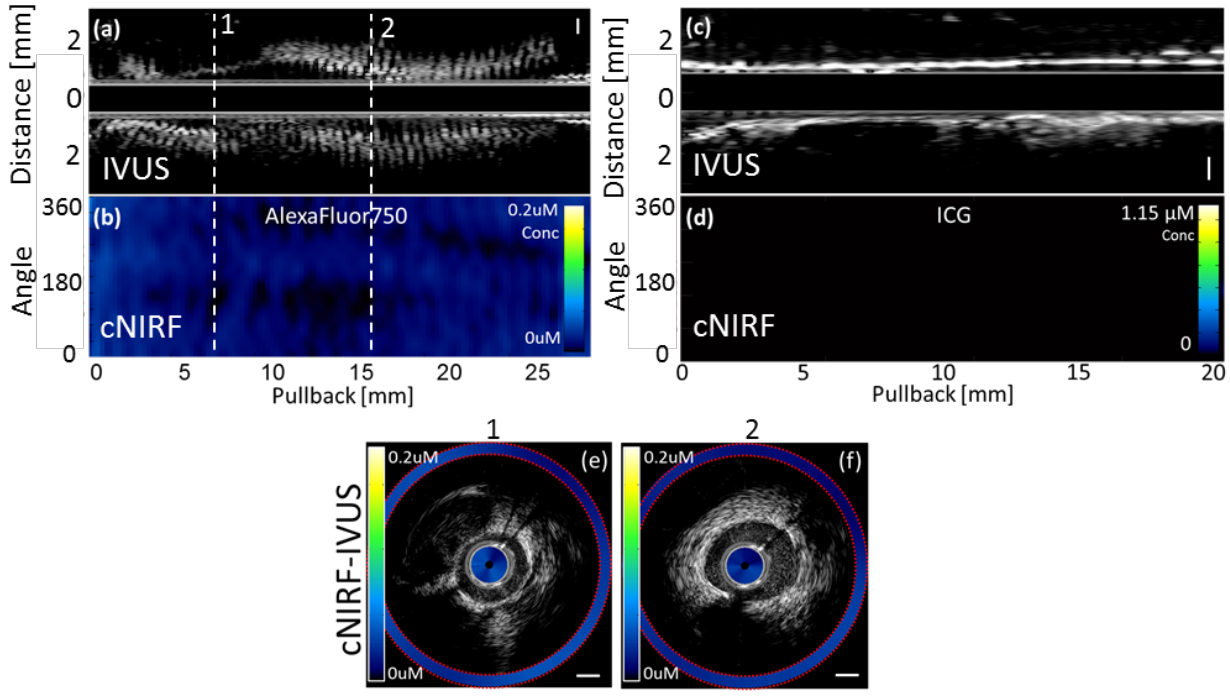

Supplemental Figure 5

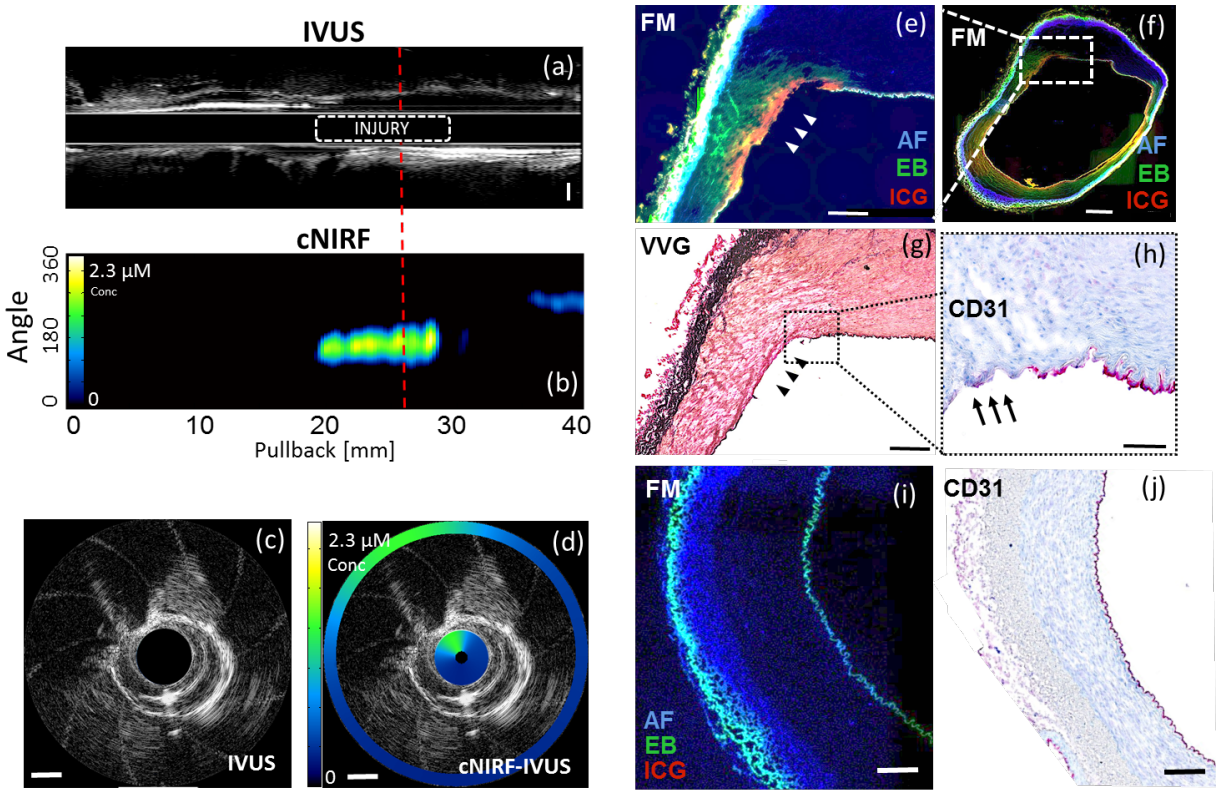

Supplemental Figure 6.

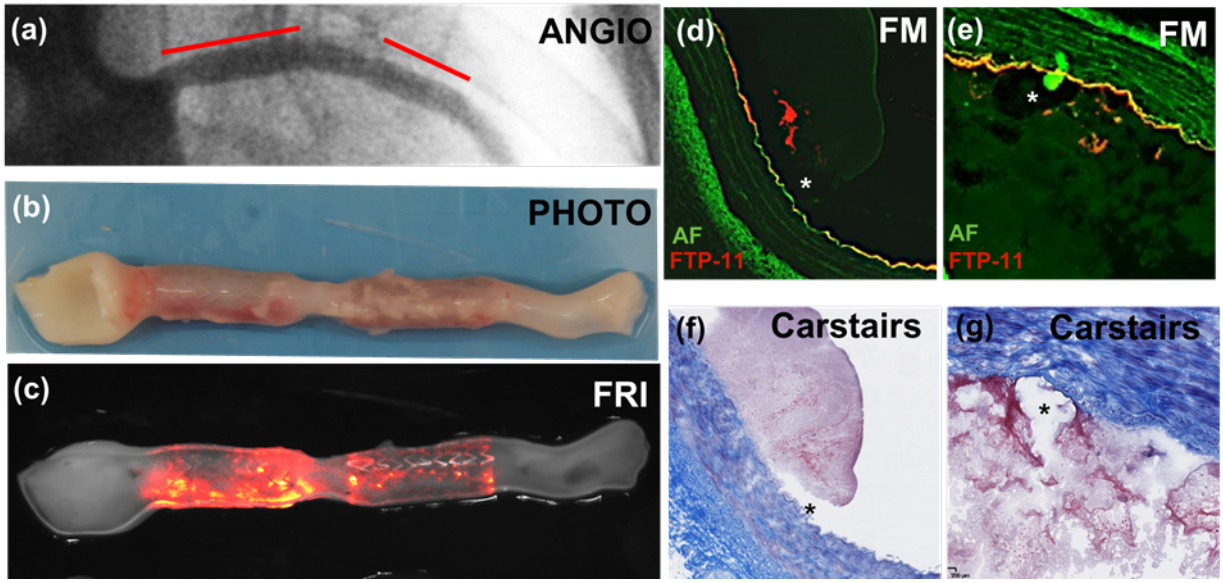

Supplemental Figure 7